View metadata, citation and similar papers at core.ac.uk
brought to you by CORE
provided by Universidade do Minho: RepositoriUM

MODEL FOR THE ANALYSIS OF STEEL FIBRE REINFORCED CONCRETE SLABS ON GRADE

J. A. O. Barros[1] and J. A. Figueiras[2]

[1] Dep. of Civil Eng., School of Eng., Univ. of Minho, Azurém, 4810 058 Guimarães, Portugal

[2] Dep. of Civil Eng., Faculty of Eng., Univ. of Porto, Rua dos Bragas, 4050 123 Porto, Portugal

Summary

A constitutive model is developed for material non-linear analysis of steel fibre reinforced concrete slabs supported on soil. The energy absorption capacity provided by fibre reinforcement is taken into account in the material constitutive relationship. The theory of plasticity is used to deal with the elasto-plastic behaviour of concrete. A smeared-crack model is used for reproducing the concrete cracking behaviour. The soil non-linear behaviour is simulated by springs on orthogonal direction to the slab. The loss of contact between the slab and the soil is accounted for. The model performance is assessed using results of experimental research.

KEY WORDS: steel fibres, elasto-plasticity, smeared-crack model, fracture energy, softening, finite element method

1 - INTRODUCTION

Westergaard [1] was, probably, the first researcher to develop analytical models for studying plain concrete beams and slabs supported on an elastic field. These models are, however, restricted to the linear elastic regime, which is far from the real behaviour of cement based materials such as concrete. In order to avoid the brittle failure of plain concrete, the use of steel rods and steel wire meshes on concrete industrial floors became a current practice after the sixties. To design reinforced concrete slabs on grade, Losberg [2] and Meyerhof [3] developed analytical models based on the yield line theory [4]. However, these models are not able to reproduce the deformational behaviour up to the collapse load of a reinforced concrete slab on grade.

Recently, a finite element based model [5] was proposed to evaluate the load-carrying capacity of plain concrete slabs on grade. However, the model results are mesh dependent [6] because the tensile post cracking energy absorption capacity was not accounted for.

In the last two decades the conventional reinforcement on industrial floors has been replaced by steel fibres. Research and practice have shown that, in comparison to conventional reinforcement, steel fibre reinforcement is more efficient and economic for industrial floors [7,8]. The mechanical properties and the cracking behaviour are improved by adding steel fibres to the concrete mix [9-11]. Numerical models for analysing laminar structures of steel fibre reinforced concrete (SFRC) are still scarce. Using a model for material non-linear analysis of reinforced concrete structures, Falkner and Teutsch [12] have proposed some procedures to adjust this model to SFRC structures. The main suggestion advanced by these researchers was the evaluation of a reinforcement equivalent

to a given content of fibres. This procedure was based on the equivalent flexural tensile strength proposed by the German Concrete Association [13]. The assumptions of Falkner and Teutsch seem too simplified for simulating the behaviour introduced by fibre reinforcement, as it can be observed from their numerical results.

The experimental research has revealed that the post-peak behaviour of SFRC, both under tension and under compression is much more ductile than the corresponding behaviour of plain concrete [9,14]. New constitutive laws have been proposed for modelling the post-peak behaviour of SFRC in compression, as well as in tension [10]. The failure envelope of SFRC under biaxial compression is also different from the corresponding plain concrete [15,16]. However, for the content of fibres usually applied in industrial floors, the differences are marginal.

In the present work a constitutive model is developed for material non-linear analysis of SFRC slabs supported on soil. The main characteristics induced by fibre reinforcement are simulated in the material constitutive laws, namely, in the tension and in the compression post-peak stress-strain relationship. The parameters of the material constitutive laws have been assessed for concrete reinforced with hooked ends steel fibres [17] (ZP30/.50 and ZX60/.80).

2 – THE SOFTENING BEHAVIOUR OF SFRC

2.1 - Introduction

The ability of SFRC to absorb energy has long been recognized [9,18-20] as one of the most important benefits of incorporating fibres into plain concrete. Tension [21], compression [22-23] and bending [9,10] tests performed under displacement control have revealed the high-energy absorption capacity of SFRC. For the content of fibres used in current applications the tension and the compression behaviour are basically changed on their post-peak branches (strain-softening).

An experimental work was recently carried out to appraise the strain softening behaviour of SFRC on tension and on compression [10]. The main results obtained and used in ascertaining the numerical model developed, will be briefly described in the present section.

2.2 – Compression behaviour

Previous work [14,22,23] has shown that the complete stress-strain expressions proposed for plain concrete [24,25] cannot adequately fit the post-peak response of the fibre concrete. Based on experimental research, a new expression was proposed [10],

$$\sigma_c = f_c \frac{\frac{\varepsilon_c}{\varepsilon_{c1}}}{(1-p-q)+q\left(\frac{\varepsilon_c}{\varepsilon_{c1}}\right)+p\left(\frac{\varepsilon_c}{\varepsilon_{c1}}\right)^{\frac{1-q}{p}}} \tag{1}$$

with

$$q = 1-p-\frac{E_{c1}}{E_{ci}}, \quad p+q \in]0,1[, \quad \frac{1-q}{p} > 0 \tag{2}$$

where

$$\varepsilon_{c1} = \varepsilon_{c10} + 0.0002 W_f, \tag{3}$$

$$p = 1.0 - 0.919 \exp(-0.394 W_f) \tag{4}$$

for *ZP30/.50* fibres and

$$\varepsilon_{c1} = \varepsilon_{c10} + 0.00026 W_f, \tag{5}$$

$$p = 1.0 - 0.722 \exp(-0.144 W_f) \tag{6}$$

for *ZX60/.80* fibres. In these expressions f_c is the compression strength, E_{ci} is the initial modulus of elasticity, E_{c1} is the modulus of elasticity at peak stress [24], ε_{c10} is the strain at peak for plain concrete (2.2×10^{-3} according to CEB-FIP Model Code 1990) and W_f is the fibre weight percentage in the mixture. In Fig. 1, $\sigma_c - \varepsilon_c$ experimental curves are compared to the $\sigma_c - \varepsilon_c$ relationship given by the above expressions [10].

2.3 – Post peak tensile behaviour

Four point bending tests under displacement control were carried out on notched beams [14] to assess the post cracking behaviour and to evaluate the fracture energy [26] of SFRC. Fibre content of 0, 30, 45 and 60 kg/m^3, concrete compression strength between 30 to 60 MPa and fibre aspect ratio (ratio between the fibre length, ℓ_f, and the fibre diameter, d_f) of 60 and 75 were the main variables analysed. Based on the results obtained, the following expressions were proposed for evaluating the fracture energy

$$\frac{G_f}{G_{fo}} = 19.953 + 3.213 W_f \tag{7}$$

for concrete reinforced with *ZP30/.50* fibres and

$$\frac{G_f}{G_{fo}} = 1.0 + 13.159 W_f^{1.827}, \tag{8}$$

for concrete reinforced with *ZX60/.80* fibres, where G_{fo} is the fracture energy of the corresponding plain concrete, which can be evaluated from RILEM recommendations [26].

The shape of the tensile strain-softening diagram of *SFRC* was obtained by performing numerical simulations of the tests. This numerical simulation revealed [14] that a trilinear diagram (see Fig. 2 and Table 1) is appropriate to reproduce the post-peak tensile behaviour of *SFRC*.

The values of the characteristic points of the trilinear softening diagram, specified in Table 1, were also obtained from the numerical simulation of the tests.

Table 1. Values for defining the characteristic points of the softening diagram of *SFRC*.

Parameters	Fibre type					
	ZP30/.50			ZX60/.80		
	Fibre content (kg/m^3)			Fibre content (kg/m^3)		
	30	45	60	30	45	60
$\xi_1 \left(\times 10^{-3}\right)$	7 – 9	4 - 6	3 - 5	3 - 5	3 - 5	10 - 100
α_1	0.35 - 0.45	0.55 – 0.65	0.6 – 0.65	0.4 – 0.5	0.6 – 0.7	0.65 – 0.75
ξ_2	0.2 – 0.3	0.25 – 0.35	0.3 – 0.4	0.15 – 0.25	0.15 – 0.25	0.3 – 0.5
α_2	0.1 – 0.2	0.15 – 0.25	0.15 – 0.25	0.2 – 0.3	0.25 – 0.35	0.25 – 0.35

3 – NUMERICAL MODEL

3.1 - Introduction

In order to simulate the progressive damage induced by plasticity and cracking, the concrete shell element thickness is discretized in layers. Each layer is considered in a state of plane stress. The concrete shell can be reinforced with conventional smeared steel bars or/and steel fibres. The shell element is formulated under the Reissner-Mindlin theory [27], using the finite element techniques [14].

The concrete cracking is simulated under the framework of the smeared crack concepts, which can be categorised into fixed, multifixed and rotating crack models [14, 28-30]. These three models are available in the computational code developed.

According to the present model, the total strain increment of cracked concrete, $\Delta\underline{\varepsilon}$, consists of the strain increment in the fracture zone, $\Delta\underline{\varepsilon}^{cr}$, and the strain increment of concrete between cracks, $\Delta\underline{\varepsilon}_{ep}^{co}$,

$$\Delta\underline{\varepsilon} = \Delta\underline{\varepsilon}_{ep}^{co} + \Delta\underline{\varepsilon}^{cr} . \tag{9}$$

In smeared crack models the fracture is distributed over a crack band width, ℓ_b, which is related to the particular finite element configuration. In the present numerical simulation ℓ_b is taken equal to the square root of the area of a Gauss point [31].

3.2 - Concrete constitutive laws

Stress and strain increment vectors are related by

$$\Delta\underline{\sigma}=\underline{D}^{co}\Delta\underline{\varepsilon}^{co} \tag{10}$$

where $\underline{D}^{co}$ is the concrete tangent constitutive matrix,

$$\underline{D}^{co}=\begin{bmatrix} \underline{D}_{mb}^{co} & \underline{\phi} \\ \underline{\phi} & \underline{D}_{s}^{co} \end{bmatrix}, \tag{11}$$

$\underline{D}_{mb}^{co}$ is the material in-plane stiffness matrix and $\underline{D}_{s}^{co}$ is the material out-of-plane shear stiffness matrix.

3.2.1 - Linear elastic uncracked concrete

For the homogeneous, isotropic and linear elastic material, the submatrix $\underline{D}_{mb}^{co}$ given in (11) is the elastic in-plane stiffness matrix, $\underline{D}_{mb,e}^{co}$,

$$\underline{D}_{mb}^{co}=\underline{D}_{mb,e}^{co}=\frac{E_{ci}}{1-\upsilon_c^2}\begin{bmatrix} 1 & \upsilon_c & 0 \\ \upsilon_c & 1 & 0 \\ 0 & 0 & \dfrac{1-\upsilon_c}{2} \end{bmatrix} \tag{12}$$

where υ_c is the concrete Poisson coefficient. The transverse shear behaviour is considered linear elastic, being the corresponding stiffness matrix given by

$$\underline{D}_{s}^{co}=\underline{D}_{s,e}^{co}=FG_c\begin{bmatrix} 1 & 0 \\ 0 & 1 \end{bmatrix} \tag{13}$$

where G_c is the concrete shear modulus and *F=5/6* is a correction shear factor [14].

3.2.2 - Linear elastic cracked concrete

For cracked concrete with concrete between cracks in linear elastic state (*ecr*), the submatrix $\underline{D}_{mb}^{co}$ given in (11) is designated by $\underline{D}_{mb,ecr}^{co}$, defined by the following expression [30]:

$$\underline{D}_{mb}^{co} = \underline{D}_{mb,ecr}^{co} = \left\{ \underline{D}_{mb,e}^{co} - \underline{D}_{mb,e}^{co} \underline{\hat{R}} \left[\underline{\hat{D}}^{cr} + \underline{\hat{R}}^{T} \underline{D}_{mb,e}^{co} \underline{\hat{R}} \right]^{-1} \underline{\hat{R}}^{T} \underline{D}_{mb,e}^{co} \right\}, \tag{14}$$

where $\underline{\hat{R}}$ is a matrix defining the direction of the cracks formed at a sampling point (Fig. 3) and $\underline{\hat{D}}^{cr}$ is a matrix which accounts for the constitutive law of the cracks. Each crack is governed by the following constitutive relationship:

$$\Delta \underline{s}^{cr} = \underline{D}^{cr} \Delta \underline{e}^{cr}, \tag{15}$$

where $\Delta \underline{s}^{cr}$ is the crack stress increment vector (Fig. 3)

$$\Delta \underline{s}^{cr} = \left[\Delta s_{nn}^{cr} \quad \Delta s_{nt}^{cr} \right]^{T}, \tag{16}$$

$\Delta \underline{e}^{cr}$ is the crack strain increment vector

$$\Delta \underline{e}^{cr} = \left[\Delta e_{nn}^{cr} \quad \Delta \gamma_{nt}^{cr} \right]^{T} \tag{17}$$

and

$$\underline{D}^{cr} = \begin{bmatrix} D_I^{cr} & 0 \\ 0 & D_{II}^{cr} \end{bmatrix}, \tag{18}$$

is the crack stiffness matrix, where D_I^{cr} and D_{II}^{cr} are the fracture mode I and the fracture mode II stiffness modulus of smeared cracks, respectively. The D_I^{cr} is characterised by the fracture parameters [6, 30], namely, the tensile strength, f_{ct}, the fracture energy, G_f, the shape of the softening law and the crack band width, l_b. Fibre reinforcement mechanisms are reflected, mainly, on the fracture energy and on the shape of the softening branch. For current fibre contents used in the concrete applications, the remainder fracture parameters are only marginally affected by fibre addition. The fracture energy and the shape of the softening branch of SFRC were evaluated from the data presented in section 2.3.

Residual strain at crack closing is higher on fibrous concrete than on plain concrete [21]. To model this behaviour it is proposed the following relationship (Fig. 2):

$$e_{nn,l}^{cr} = \eta \, e_{nn,m}^{cr}, \tag{19}$$

where $e_{nn,m}^{cr}$ is the maximum attained crack strain normal to the crack and η is given by,

$$\eta = \left[1 - \exp\left(-1000\, e_{nn,m}^{cr}\right)\right]\left[1 - \exp\left(-\frac{W_f}{C}\frac{\ell_f}{d_f}\right)\right]. \tag{20}$$

A value of 165 can be advanced to *C* parameter, but more experimental research is needed to calibrate this parameter. According to this expression, the residual strain increases with

$e_{nn,m}^{cr}$ and with the fibre percentage and fibre aspect-ratio, which is in accordance with the trend showed by the reduced experimental data available.

The fracture mode II modulus, D_{II}^{cr}, is obtained from the expression [30]:

$$D_{II}^{cr} = \frac{\beta}{1-\beta} G_c, \tag{21}$$

where β is the shear retention factor determined from

$$\beta = \left[1 - \frac{e_{nn}^{cr}}{e_{nn,u}^{cr}} \right]^p \quad (p=1, 2 \text{ or } 3) \tag{22}$$

for plain concrete, with $e_{nn,u}^{cr}$ being the ultimate normal crack strain (Fig. 2), and

$$\beta = \exp\left(-\frac{M}{W_f} \frac{d_f}{l_f} \frac{e_{nn}^{cr}}{e_{nn,u}^{cr}} \right) \tag{23}$$

for *SFRC*. Taking into account the experimental data available [32], it is proposed a value of 980 for the *M* parameter. According to this expression, the shear retention factor increases with the fibre percentage and with the fibre aspect-ratio, and decreases with the crack strain, which gives the trend revealed by the experimental data.

The shear retention factor for the conventionally reinforced concrete is evaluated from the expression proposed by Cervenka [31]

$$\beta = -\frac{\ln\left(\frac{e_{nn}^{cr}}{C_1}\right)}{C_2} \tag{24}$$

with

$$C_1 = 7 + 5\frac{\rho_{eq,ef} - 0.005}{0.015}, \quad C_2 = 10 - 2.5\frac{\rho_{eq,ef} - 0.005}{0.015}, \tag{25}$$

where $\rho_{eq,ef}$ is the equivalent effective reinforcement [14],

$$\rho_{eq,ef} = \sum_{i=1}^{nr} \rho_{i,ef} \cos^4 \theta_i \tag{26}$$

nr is the number of sets of reinforcing layers crossing the crack, $\rho_{i,ef}$ is the effective reinforcing ratio [24] of layer *i* and θ_i is the angle between the reinforcing layer *i* and the crack direction.

3.2.3 - Elasto-plastic uncracked concrete

For elasto-plastic (*ep*) uncracked concrete, the in-plane material stiffness matrix $\underline{D}_{mb}^{co}$ given in (11) is defined by

$$\underline{D}_{mb}^{co} = \underline{D}_{mb,ep}^{co} = \underline{D}_{mb,e}^{co} - \frac{\underline{D}_{mb,e}^{co}\,\underline{a}\,\underline{a}^T\,\underline{D}_{mb,e}^{co}}{h + \underline{a}^T\,\underline{D}_{mb,e}^{co}\,\underline{a}} \tag{27}$$

where $\underline{a}$ is the flow vector and h is the hardening modulus [33]. The hardening modulus depends on the equivalent stress-plastic strain relationship used for concrete in compression.

In the plasticity approach, concrete strain, ε^{co}, is decomposed into an elastic, ε_e^{co}, and a plastic, ε_p^{co}, contribution. Inserting this decomposition into the expression (1) holds

$$\sigma_c\left(\frac{q}{\varepsilon_{c1}^{co}}\varepsilon_p^{co}+A-\frac{f_c}{B}\right)+\sigma_c^2\frac{q}{B}+\sigma_c\, p\left(\frac{\sigma_c}{B}+\frac{\varepsilon_p^{co}}{\varepsilon_{c1}^{co}}\right)^{\left(1+\frac{A}{p}\right)}-f_c\frac{\varepsilon_p^{co}}{\varepsilon_{c1}^{co}}=0 \tag{28}$$

with

$$A=\frac{E_{c1}}{E_{ci}},\quad q=1-p-A,\quad B=E_{ci}\varepsilon_{c1}^{co}. \tag{29}$$

For a given concrete plastic strain, the concrete stress is computed from (28) using the Newton-Raphson method. The concrete hardening modulus is obtained by deriving Eq. (28) in order to the plastic strain.

For the fibre contents used in industrial floors, experimental research has shown [15,16] that the shape of the yield surface of *SFRC* under biaxial stress state is similar to the yield surface of the corresponding plain concrete. The yield surface proposed by Figueiras [34]

$$f_c\left(\underline{\sigma}_c,k_c\right)=\left(\underline{\sigma}_c^T\,\underline{P}_c\,\underline{\sigma}_c\right)^{1/2}+\underline{p}_c^T\,\underline{\sigma}_c-\overline{\sigma}_c\left(k_c\right)=0 \tag{30}$$

is used in the present work for plain and fibrous concrete, where $\overline{\sigma}_c\left(k_c\right)$ is the equivalent compressive stress, with k_c being the hardening parameter associated to the equivalent plastic strain rate or to the plastic work rate, $\underline{P}_c$ is the projection matrix [35]

$$\underline{P}_c = \begin{bmatrix} a & b & b & 0 \\ b & a & b & 0 \\ b & b & a & 0 \\ 0 & 0 & 0 & c \end{bmatrix} \tag{31}$$

and $\underline{p}_c$ is the projection vector,

$$\underline{p}_c = d\begin{bmatrix} 1 & 1 & 1 & 0 \end{bmatrix}^T . \tag{32}$$

Scalar parameters *a*, *b*, *c* and *d* are defined as

$$a = \left(\frac{0.355}{2}\right)^2 ,\ b = \left(\frac{0.355}{2}\right)^2 - \frac{1.355}{2} ,\ c = 3 \times 1.355 ,\ d = \frac{0.355}{2} . \tag{33}$$

3.2.4 - Elasto-plastic cracked concrete

For cracked concrete with concrete between cracks in elasto-plastic behaviour (*epcr*) the submatrix $\underline{D}_{mb}^{co}$ given in (11) is obtained from the following expression:

$$\underline{D}_{mb}^{co} = \underline{D}_{mb,epcr}^{co} = \left\{ \underline{D}_{mb,ep}^{co} - \underline{D}_{mb,ep}^{co} \hat{\underline{R}} \left[\hat{\underline{D}}^{cr} + \hat{\underline{R}}^T \underline{D}_{mb,ep}^{co} \hat{\underline{R}} \right]^{-1} \hat{\underline{R}}^T \underline{D}_{mb,ep}^{co} \right\} \tag{34}$$

where $\underline{\underline{D}}^{co}_{mb,ep}$ was defined in Eq. (27).

3.2.5 –Tensile behaviour of reinforced concrete layers

The relative position between a concrete layer and a reinforcing layer defines which diagram will be used to simulate the tensile behaviour of the concrete layer. The behaviour of a concrete layer will be simulated by a tension stiffening diagram if its middle surface is positioned within the effective tension area [24] (Fig. 4). The behaviour of the other concrete layers will be simulated by a softening diagram (Section 2.3).

A tension-stiffening model was developed [14] for laminar concrete structures reinforced with sets of smeared steel bars. These sets can have different orientation and properties. The model is based on the principles proposed by Link *et al.* [36] and Massicotte *et al.* [37], and can be represented by the post-peak stress-strain trilinear diagram illustrated in Fig. 5. The expressions defining the coordinates of the points A, B and C were deduced in a previous work [14].

3.3 - Constitutive relationship for the reinforcement

Reinforcement of smeared steel bars added to plain or fibrous concrete can be modelled by a linear-parabola diagram or by a multilinear diagram [14]. The material non-linear behaviour of steel bars is reproduced under the elasto-plasticity framework [14].

3.4 - Soil

The soil is simulated by springs orthogonal to the laminate structure (Figure 6). The tangent soil reaction modulus is usually evaluated from plate-loading tests [11]. The results of these tests have revealed that soil pressure–soil settlement relationship may be simulated by a multilinear or linear-parabola diagram [14]. The soil contribution to the stiffness of the whole structural system is computed by adding the soil stiffness matrix,

$$\underline{\underline{K}}_{so}^{(e)} = \int_{A^{(e)}} \underline{N}^T k_s \underline{N} dA \tag{35}$$

to the slab stiffness, where $A^{(e)}$ is the area of a finite element, $\underline{N}$ is a vector with the dimension of the number of element nodes. The terms of $\underline{N}$ are the values of the element shape functions. In Eq. (35) k_s is the tangent soil reaction modulus. The soil stiffness contributes only to the rigidity terms of the degrees-of-freedom orthogonal to the laminate structure. The friction between the slab and the soil is neglected.

If in a given sampling point the concrete slab loses the contact with the soil (Fig. 7), i.e., if the displacement orthogonal to the slab middle surface, u_3, is less than the plastic soil settlement, a_{sp}, the part of the soil corresponding to this sampling point does not contribute to the stiffness of the slab-soil system. These procedure accounts for the zones where the soil has plastic settlements (zone A in Fig. 7), as well as, for the zones where the slab lift up with soil in linear elastic state (zone B in Fig. 7).

4 - MODEL APPRAISAL

In a previous work [11] the model performance was already assessed, simulating the tests carried out with sets of slabs of plain concrete, slabs reinforced with wire mesh and slabs reinforced with 30 and 45 kg/m^3 of ZX60/.80 hooked ends steel fibres. The purpose of the present section is to evaluate the model performance by simulating the behaviour of SFRC slabs supported on other materials such as rubber and cork. For experimental research in laboratory, these materials are easier to deal with than soil, being a useful alternative.

Falkner and Teutsch [12] have carried out tests with 3000×3000×150 mm concrete slabs supported on a 60 mm thick elastic subbase of cork and rubber. The slabs were loaded via a hydraulic jack, acting on a 120×120 mm^2 steel plate placed at the centre of the slab. The two experimental tests carried out with concrete slabs reinforced with 20 kg/m^3 of 60/.80 hooked ends Dramix steel fibres [17] are simulated with the numerical model described in the present work. The slab designated by P3 was supported on elastic cork subbase. In slab named P4, the elastic cork subbase was replaced by a layer of rubber mats of the same thickness, in the load applied zone over an area of 1.5×1.5 m^2. The reaction modulus of the cork and rubber subbase was evaluated from plate loading tests on specimens of 500×500 mm, with a plate of 150 mm diameter. The values of the material properties for numerical simulation are included in Table 2. These values were obtained from the experimental data published [12] (see also Fig. 8).

Taking the symmetry of the problem, a quarter of the slab is discretized by eight-noded isoparametric Serendipity elements, as shown in Fig. 9. The slab thickness is discretized in

10 layers of equal thickness. The stiffness and the internal forces of the slab-soil structural system are evaluated using 2×2 Gauss points per finite element.

Table 2. Values of the material properties.

Concrete (Fig. 2)			**Soil (Fig. 8)**	
Common data for P3 and P4 slabs	**Specific data for P3 slab**	**Specific data for P4 slab**	**Cork subbase**	**Rubber subbase**
υ =0.15 ε_{co} =2.2×10^{-3} W_f =0.83 α_1 =0.4 ξ_1 =0.005 α_2 =0.25 ξ_2 =0.1	E_{ci} =31000MPa f_c =35 MPa f_{ct} =2.5 MPa G_f =0.75 N/mm	E_{ci} =32500MPa f_c =40 MPa f_{ct} =3.0 MPa G_f =0.83 N/mm	k_{sl} =0.035 N/mm^3 p_{s1} =0.1 MPa k_{s1} =0.03 N/mm^3 p_{s2} =0.25 MPa k_{s2} =0.025 N/mm^3 p_{su} =0.5 MPa	k_{sl} =0.055 N/mm^3 p_{s1} =0.1 MPa k_{s1} =0.05 N/mm^3 p_{s2} =0.4 MPa k_{s2} =0.045 N/mm^3 p_{su} =1.0 MPa

In Figs 10 and 11, the experimental and the numerical load-central deflection relationship for the slabs P3 and P4 are illustrated. The comparison with the experimental data shows a very good agreement.

Figs 12 and 13 represent the deflection of slabs P3 and P4 along the x_1 axis (Fig. 9) for the selected loading levels. The deflection is not symmetric due to the non-symmetric crack pattern observed in the experiments. The deflection shape of slab P3 is predicted quite well for all the load levels, except for 220 kN load level. Observing the force-deflection

relationship of slab P3 (Fig. 10), it is noted that, above the load of 220 kN, the deflection increases significantly for a small load increment. Due to this fact, the deflection for load level of 230 kN is also included in Figure 12. It can be conclude that the deflection registered experimentally for 220 kN is reproduced with reasonable accuracy in the range 220-230 kN in the numerical simulation.

In slab P4, apart from the left branch of the deflection along the x_1 axis for load level of 345 kN, the remainder deflections are predicted quite well. The smaller deflection predicted by the numerical model in $-1500 \leq x_1 \leq 0$ mm for load level of 345 kN (Fig. 13) is due to the crack pattern developed in the experiment [12]. The deflection in the negative x_1 coordinate is smaller, because the failure crack nº 3 (Figure 14) is far from the x_1 axis comparing to the failure crack nº 1. The direction of the crack nº 1 is similar to the direction of the rupture crack determined by the numerical model, as it can be observed in Figs 14 and 15. In Fig. 15, only the cracks completely open (where the fracture energy was exhausted) are depicted. A crack is represented by a rectangle with thickness proportional to crack opening ($e_{nn}^{cr} \ell_b$)

The deflections registered on displacement transducers placed at corners (50 mm apart from the corner – point P in Fig. 9) in slab P3 for load levels of 60, 120, 180 and 220 kN are depicted in Fig. 16. The relationship between the applied force and the displacement at point P obtained with the numerical model is also illustrated in Fig. 16. A good agreement between experimental and numerical results is observed.

4 - CONCLUSIONS

A numerical model for the non-linear analysis of steel fibre reinforced concrete slabs supported on soil was developed. Using experimental data, the main features of the fibre reinforcement were introduced in the concrete constitutive laws, mainly in the tension and in the compression post-peak behaviour. More experiments should be carried out in order to tune the constitutive laws proposed. The experimental research performed was restricted to two types of fibres only.

The behaviour of the uncracked concrete and concrete between cracks was simulated under the elasto-plasticity framework. The cracking behaviour was reproduced using a smeared multifixed crack model. The soil or other base material supporting the concrete slab was simulated by distributed springs orthogonal to the concrete slab middle surface. An elasto-plastic model was used to modulate the non-linear behaviour of the springs. The loss of contact between the base and the slab was accounted for.

The model performance was evaluated using the experimental results given by Falkner and Teutsch. A good agreement between the experimental and the numerical results was obtained.

5 - REFERENCES

1. Westergaard, H.M., New formulas for stresses in concrete pavements of airfield. *Transactions of ASCE*, 1948, **113**(2340), 425-444.

2. Losberg, A., *Design methods for structurally reinforced concrete pavements*, Transactions of Chalmers University of Technology Gothenburg, Sweden, 1961.

3. Meyerhof, G.G., Load carrying capacity of concrete pavements. *Jour. Soil Mech. and Found. Div.*, ASCE, 1962, **88**(3), 89-115.

4. Baumann, R.A. and Weisgerber, F.E., Yield line analysis of slabs-on-grade. *Jour. Struct. Engrg.* ASCE, 1983, **109**(7), 1553-1568.

5. Shentu, L., Jiang, D. and Hsu, C.-T.T., Load-carrying capacity for concrete slabs on grade. *Jour. Struct. Engrg.*, ASCE, 1997, **123**(1), 95-103.

6. Bazant, Z.P. and Oh, B.H., Crack band theory for fracture of concrete. *Materials and Structures*, RILEM, 1983, **16**(93), 155-177.

7. Nanni, A. and Johari, A., RCC pavement reinforced with steel fibers. *Concrete International*, April 1989, 64-69.

8. Tatnall, P.C. and Kuitenbrouwer, L., Steel fiber reinforced concrete in industrial floors. *Concrete International*, December 1992, 43-47.

9. ACI 544.1R-96, *State-of-the-Art Report on Fiber Reinforced Concrete*, ACI, 1997.

10. Barros, J.A.O. and Figueiras, J.A., Flexural behavior of steel fiber reinforced concrete: testing and modelling. *Journal of Materials in Civil Engineering, ASCE.* 1999, **11**(4), 331-339.

11. Barros, J.A.O. and Figueiras, J.A., Experimental behaviour of fibre concrete slabs on soil. *Journal Mechanics of Cohesive-frictional Materials*, 1998, **3**, 277-290.

12. Falkner, H. and Teutsch, M., *Comparative investigations of plain and steel fibre reinforced industrial ground slabs*, Institut fur Baustoffe, Massivbau und brandschutz, 1993, nº 102.

13. German Concrete Association, *Recommendations: Fundamental Principles for the Evaluation of Steel Fibre Concrete in Tunnel Construction*, Edition September 1992.

14. Barros, J.A.O., *Comportamento do betão reforçado com fibras - análise experimental e simulação numérica*, PhD Thesis, Civil Eng. Dept., Faculty of Engineering, University of Porto, Portugal, 1995 (in Portuguese).

15. Yin, W.S., Su, E.C.M., Mansur, M.A. and Hsu, T.T.C., Biaxial Tests of plain and fiber concrete. *ACI Materials Journal*, 1989, **86**(3), 236-243.

16. Traina, L.A. and Mansour, S.A., Biaxial strength and deformational behaviour of plain and steel fiber concrete. *ACI Materials Journal*, 1991, **88**(3), 354-362.

17. *Dramix fibres hors fils d'acier pour reinforcement de betón et mortier*, Specification, Bekaert N.V., October, 1991.

18. Balaguru, P.N. and Shah, S.P., *Fiber reinforced cement composites*, McGraw-Hill International Editions, Civil Engineering Series, 1992.

19. Trottier, J.-F. and Banthia, N., Toughness characterization of steel-fiber reinforced concrete. *J. Materials Civ. Engrg.*, ASCE, 1994, **6**(2) 264-289.

20. Gopalaratnam, V.S., Shah, S.P., Batson, G.B., Criswell, M.E., Ramakrishnan, V., Wecharatana, M., Fracture toughness of fiber reinforced concrete. *ACI Materials Journal*, July-August 1991, **88**(4), 339-353.

21. Gopalaratnam, V.S. and Shah, S.P., Tensile failure of steel fibre-reinforced mortar. *Jour. of Eng. Mech., ASCE*, May 1987, **113**(5), 635-653.

22. Fanella, D.A. and Naaman, A., Stress-strain properties of fiber reinforced mortar in compression. *ACI Journal*, 1985, **82**(4), 475-483.

23. Ezeldin, A.S. and Balaguru, P.N., Normal- and high-strength fiber-reinforced concrete under compression. *J. Materials in Civil Engrg,* ASCE, 1993, **4**(4), 415-428.

24. CEB-FIP Model Code, *Design code*, Bulletin d'Information CEB Lausanne, Switzerland, 1993.

25. Wee, T.H., Chin, M.S. and Mansur, M.A., Stress-strain relationship of high-strength concrete in compression. *J. Materials Civ. Engrg.*, ASCE, 1996, **8**(2), 70-76.

26. RILEM, Draft Recommendation, 50-FMC Committee Fracture Mechanics of Concrete, Determination of fracture energy of mortar and concrete by means of three-point bend tests on notched beams. *Materials and Structures*, 1985, **18**(106), 285-290.

27. Reissner, E., The effect of transverse shear deformation on the bending elastic plates. *Jour. Appl. Mech.*, 1945, **12**, 69-76.

28. De Borst, R. and Nauta, P., Non-orthogonal cracks in a smeared finite element model. *Eng. Computations*, March 1985, **2**, 35-46.

29. De Borst, R., *Non-linear analysis of frictional materials*, Ph.D. Thesis, Delft Univ. of Technology, 1986.

30. Rots, J.G., *Computational modeling of concrete fracture*, Ph.D. Thesis, Delft Univ. of Technology, 1988.

31. Cervenka, V., Pukl, H. and Eligehausen, R., Computer simulation of anchoring technique and design of concrete structures. *Proc. Second Intern. Conf. on Computer Aided Analysis and Desing of Concrete Structures, Zell am See*, Austria, 1990, 1-19.

32. Swamy, R., Jones, R. and Chiam, T., Shear transfer in steel fiber reinforced concrete. *Fiber Reinforced Concrete Properties and Applications*, Eds: S.P. Shah, G.B. Batson, SP-105, 1987, 565-592.

33. Hofstetter, G. and Mang, H.A., *Computational mechanics of reinforced concrete structures*, Ed. Vieweg, 1995.

34. J.A. Figueiras, *Ultimate load analysis of anisotropic and reinforced concrete plates and shells*, Ph.D. Thesis, C/Ph/72/83, Uni. College of Swansea, 1983.

35. Feenstra, P.H., *Computational aspects of biaxial stress in plain and reinforced concrete*, Ph.D. Thesis Delft Univ. of Technology, 1993.

36. Link, R.A., Elwi, A.E. and Scanlon, A., Biaxial tension stiffening due to generally oriented reinforced layers. *Jour. of Eng. Mech., ASCE*, August 1989, **115**(8), 1647-1662.

37. Massicote, B., Elwi, A.E. and J.G. MacGregor, Tension-stiffening model for planar reinforced concrete members. *Jour. of Struct. Eng., ASCE*, November 1990, **116**(11), 3039-3058.

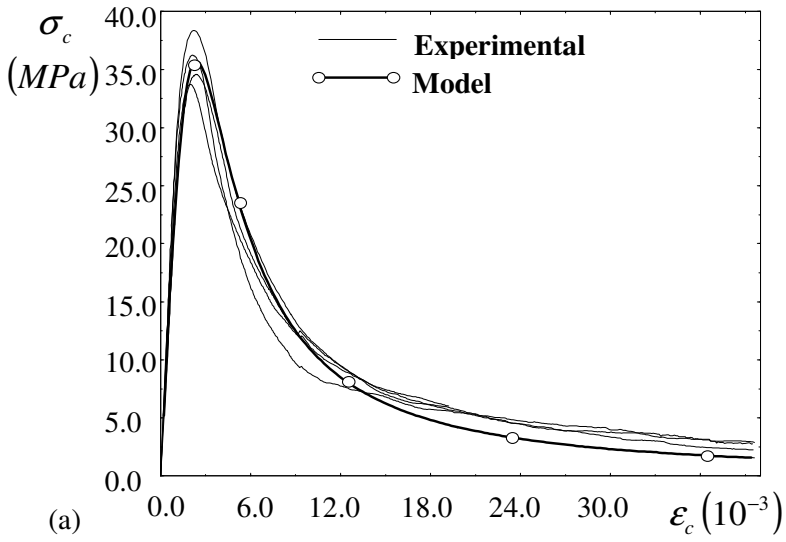

(a)

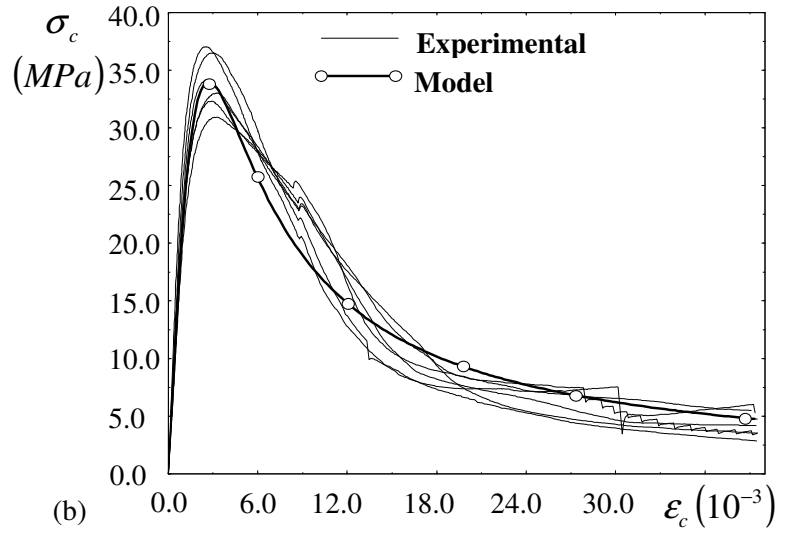

(b)

Fig. 1. Analytical versus experimental compression stress-strain curves for concrete reinforced with 30 kg/m^3 (a) and 60 kg/m^3 (b) of *ZX60/.80* fibers [10].

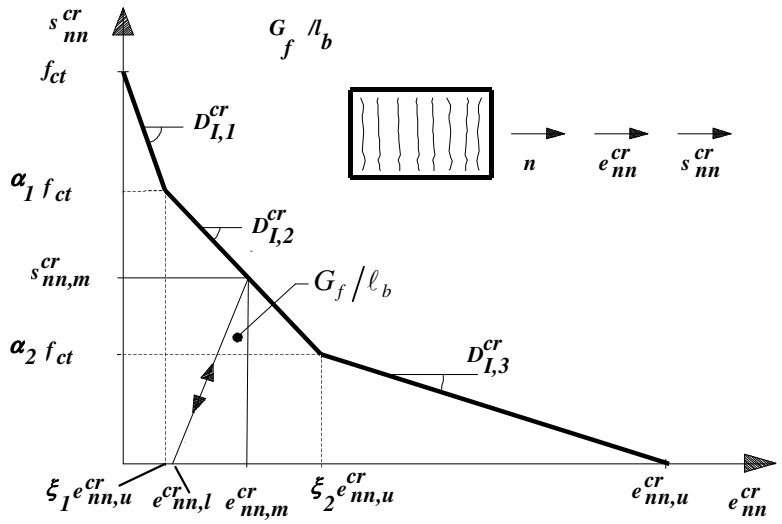

Fig. 2. Trilinear softening diagram for hooked-ends steel fibre reinforced concrete (ℓ_b is the width of the fracture process zone).

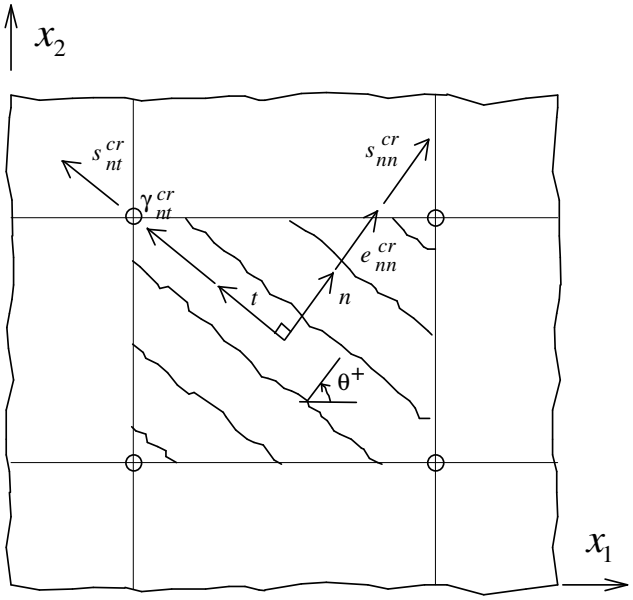

Fig. 3. Crack stress and crack strain components.

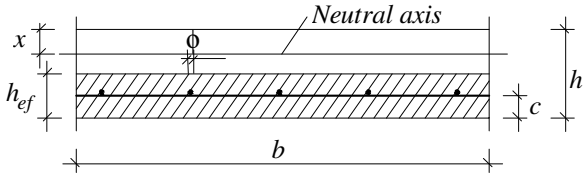

$$h_{ef} = \min\begin{cases} 2.5(c + \phi/2) \\ (h - x)/3 \end{cases}$$

Fig. 4. Effective tension area according to CEB-FIP Model Code 1990 [24].

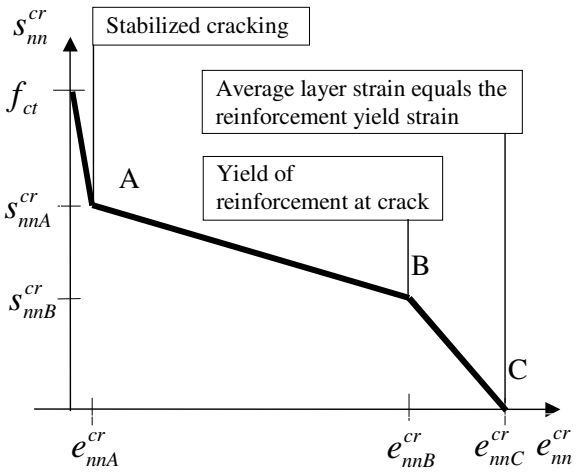

Fig. 5. Tension-stiffening diagram [14].

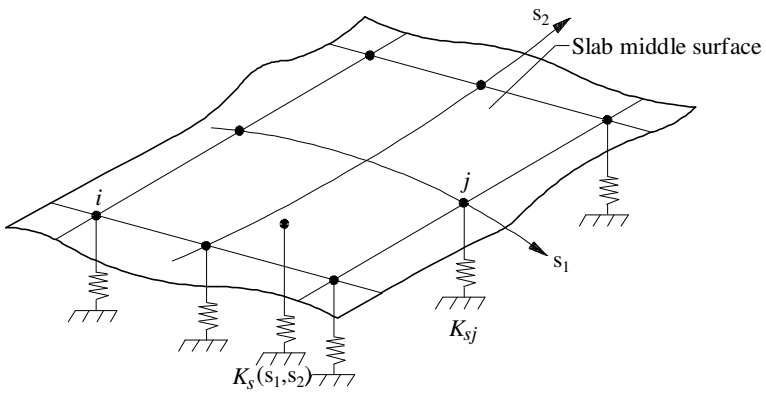

Fig. 6. The soil is simulated by spring elements, orthogonal to the concrete slab middle surface.

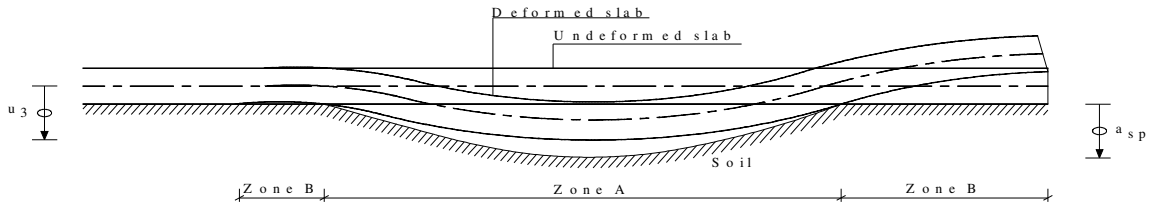

Fig. 7. The loss of contact between the slab and the soil is accounted for.

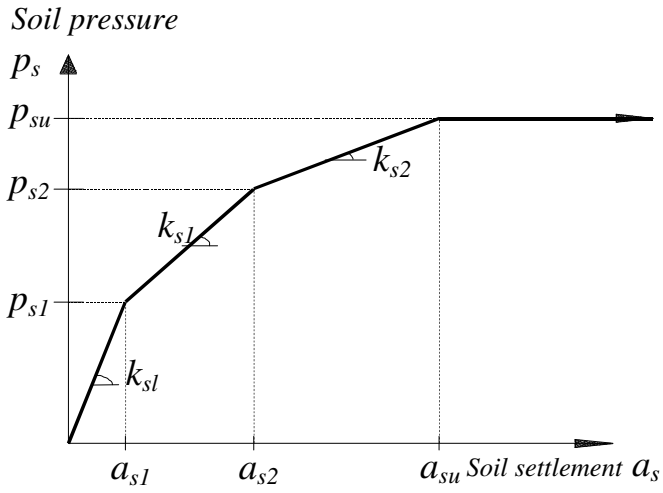

Fig. 8 - Pressure–settlement relationship used to simulate the soil behaviour.

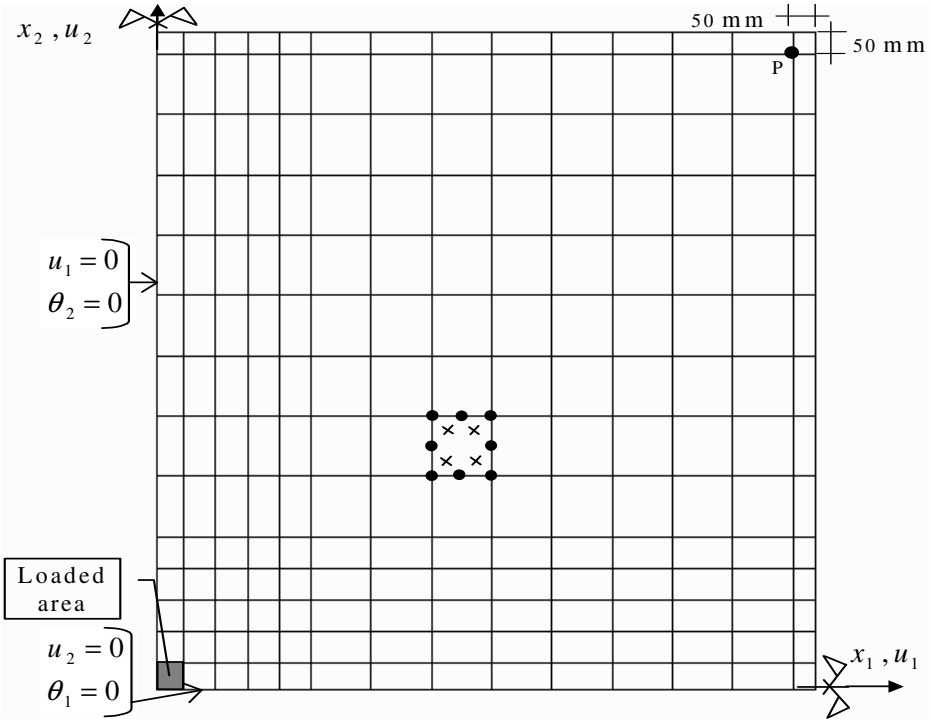

Fig. 9. Finite element mesh.

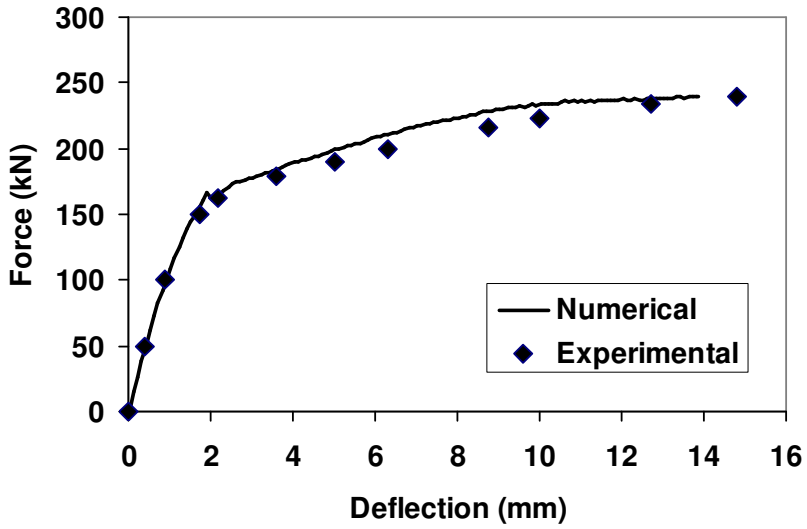

Fig. 10. Force-deflection relationship at the central point of slab P3.

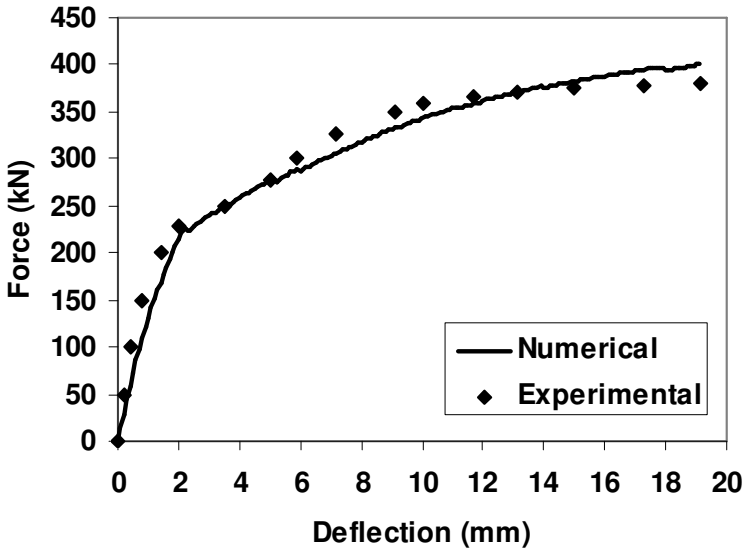

Fig. 11. Force-deflection relationship at the central point of slab P4.

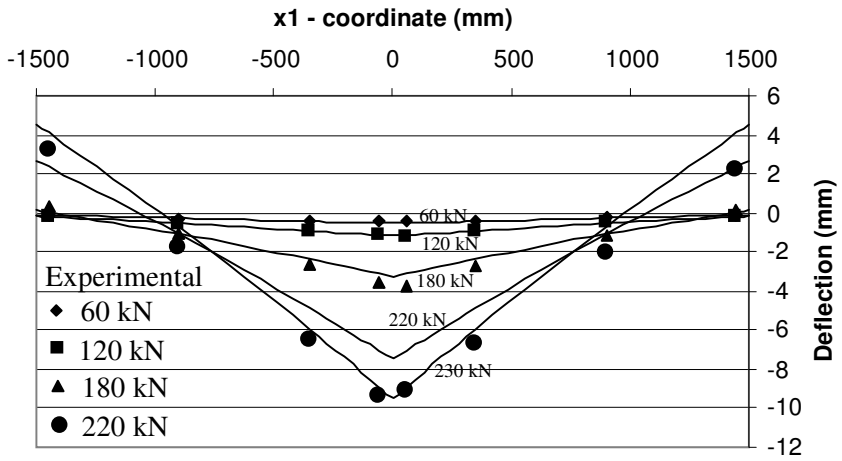

Fig. 12. Deflection of slab P3 along x_1 axis.

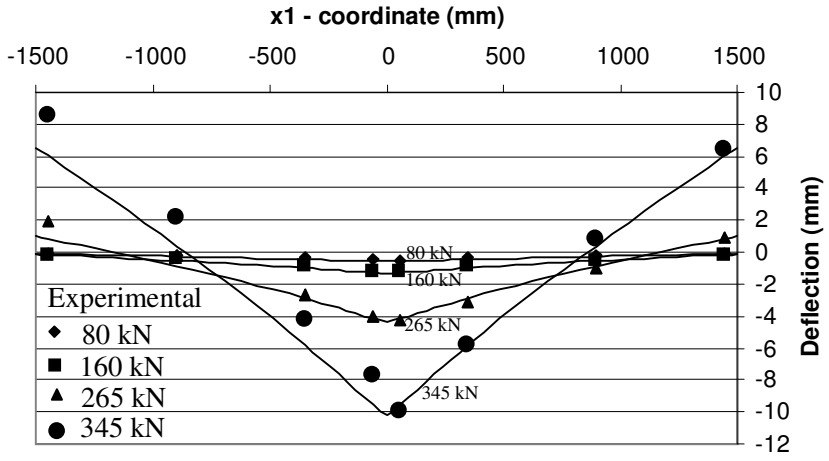

Fig. 13. Deflection of slab P4 along x_1 axis.

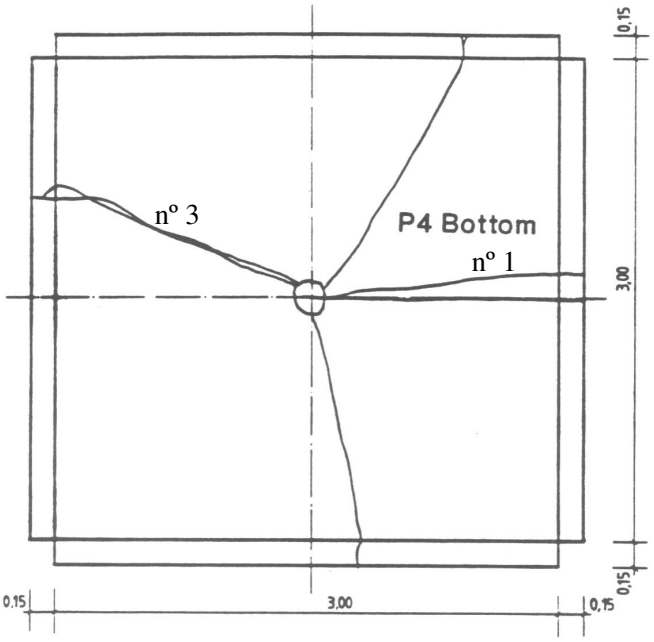

Fig. 14. Crack pattern of test slab P4 after failure (experimental).

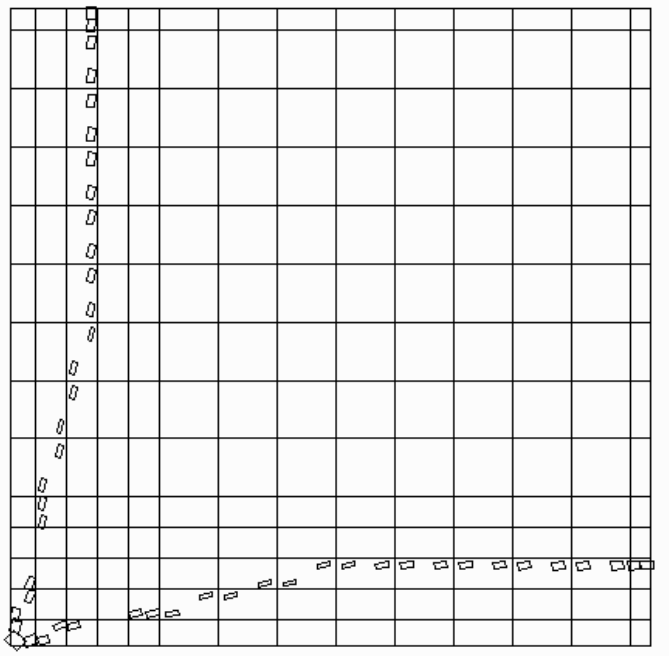

Fig. 15. Crack pattern at bottom layer of test slab P4 for ultimate load (numerical).

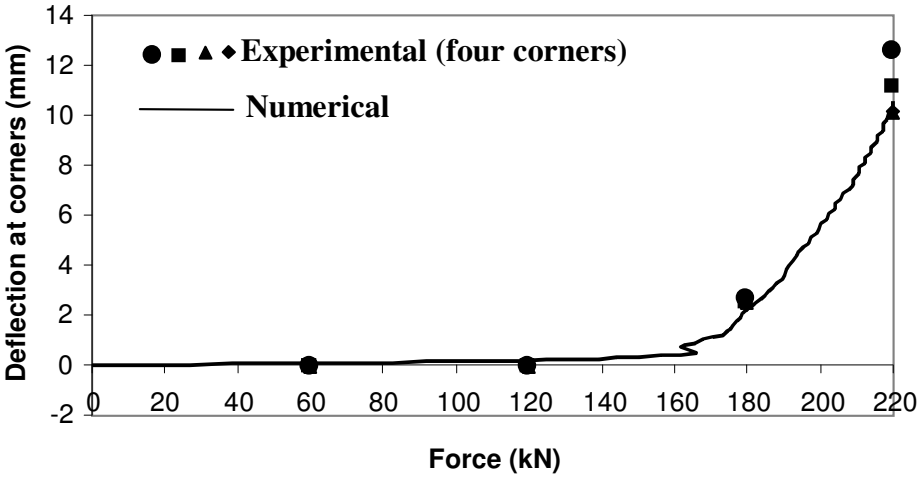

Fig. 16. Deflection at point P (Fig. 9).

Fig. 1. Analytical versus experimental compression stress-strain curves for concrete reinforced with 30 kg/m^3 (a) and 60 kg/m^3 (b) of *ZX60/.80* fibers [10].

Fig. 2. Trilinear softening diagram for hooked-ends steel fibre reinforced concrete (ℓ_b is the width of the fracture process zone).

Fig. 3. Crack stress and crack strain components.

Fig. 4. Effective tension area according to CEB-FIP Model Code 1990 [24].

Fig. 5. Tension-stiffening diagram [14].

Fig. 6. The soil is simulated by spring elements orthogonal to the concrete slab middle surface.

Fig. 7. The loss of contact between the slab and the soil is accounted for.

Fig. 8 - Pressure–settlement relationship used to simulate the soil behaviour.

Fig. 9. Finite element mesh.

Fig. 10. Force-deflection relationship at the central point of slab P3.

Fig. 11. Force-deflection relationship at the central point of slab P4.

Fig. 12. Deflection of slab P3 along x_1 axis.

Fig. 13. Deflection of slab P4 along x_1 axis.

Fig. 14. Crack pattern of test slab P4 after failure (experimental).

Fig. 15. Crack pattern at bottom layer of test slab P4 for ultimate load (numerical).

Fig. 16. Deflection at point P (see fig. 9).